Energy Storage Materials 89 (2026) 105224

Contents lists available at ScienceDirect

Energy Storage Materials

journal homepage: www.elsevier.com/locate/ensm

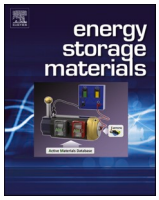

Linking ion ordering, structural dynamics, and charge storage kinetics in the tunnel structure electrode material Li_xMoO_2

Nicolas Leport [a,†], Daniel D. Robertson [b,†], Yucheng Zhou [a], Sarah H. Tolbert [b,c,d,*], Laurent Pilon [a,c,e,*]

[a] Mechanical and Aerospace Engineering Department, Henry Samueli School of Engineering and Applied Science, University of California, 420 Westwood Plaza, Los Angeles, CA, 90095, USA
[b] Department of Chemistry and Biochemistry, University of California, 607 Charles E. Young Drive East, Los Angeles, CA, 90095, USA
[c] California NanoSystems Institute, University of California, Los Angeles, USA
[d] Department of Materials Science and Engineering, University of California, Los Angeles, USA
[e] Institute of the Environment and Sustainability, University of California, Los Angeles, USA

ARTICLE INFO

Keywords:
Lithium-ion battery
Entropic potential
Intercalation
Galvanostatic intermittent titration technique
Operando calorimetry

ABSTRACT

In lithium-ion batteries, ion insertion may result in lattice expansion and phase transitions, associated with slow charging. Nanostructured battery materials exhibit faster rate capability due to finite size effects, yet this mechanism remain anecdotal. This study explains those effects using potentiometric entropy measurements to examine connections among ion ordering, structural phase transitions, and kinetics. Strong ion ordering is demonstrated in bulk tunnel-structured Li_xMoO_2 despite the presence of a single crystallographic site for lithium. The largest ion ordering event coincides with the onset of a first-order phase transition and a maximum cell overpotential. These observations suggest that the phase transition occurs to bypass the energetic minimum of the ion-ordered state slowing charge storage considerably. Then, in nanoporous MoO_2, ion ordering signatures are lessened. Accordingly, the phase transition remains first-order, but with smaller lattice mismatch and composition range of two-phase coexistence with a much smaller overpotential. Finally, in MoO_2 nanocrystals, ion ordering nearly disappears and structural evolution occurs through a second-order solution process that does not increase the overpotential. Experimental open-circuit voltage and entropic potential observed for the three types of MoO_2 were recreated with thermodynamic modeling on a three-site system with different extents of ion ordering. Finally, *operando* calorimetry confirmed dramatic reduction in energy losses and heat generation in nanostructured materials. Overall, this work provides new mechanistic understanding of the role of ion ordering during cycling by highlighting that decreased ion ordering in nanostructured materials, even when a first-order phase transition remains, enables significantly enhanced rate performance.

1. Introduction

Fast-charging Li-ion batteries (LIBs) are key to many technologies, including electric vehicles, which still have limited range and relatively long charging time compared to internal combustion engines. Currently, charging time in LIBs is limited primarily by the anode, since the most common anode material, graphite, provides high energy density but suffer from lithium plating when charged at high current densities [1]. Side reactions related to the overpotential of fast charging can also consume electrolyte, decrease cell life, and potentially lead to catastrophic cell failure [1]. A number of alternative anode materials have been proposed for fast-charging LIBs, including Wadsley-Roth shear phases [2], bronzes [3], disordered rock salt materials [4,5], and tunnel structures [6,7]. While many of these candidates show very good rate capability, further improvements are still necessary. To meet these challenging performance requirements, it is essential to understand the material parameters that enable fast charging at a fundamental level.

For a typical insertion electrode, the charging process involves redox reactions in the host material, enabled by charges introduced through the current collector, combined with (de)insertion of lithium ions to balance the charge. To achieve full capacity, lithium ions and electrons must be readily available throughout the electrode, which becomes

* Corresponding authors at: California NanoSystems Institute, University of California, Los Angeles, USA.
E-mail addresses: tolbert@chem.ucla.edu (S.H. Tolbert), pilon@seas.ucla.edu (L. Pilon).
† Contributed equally to this work.

https://doi.org/10.1016/j.ensm.2026.105224
Received 2 February 2026; Received in revised form 18 April 2026; Accepted 15 May 2026
Available online 16 May 2026

increasingly difficult at high current densities. The diffusion of ions in solid particles of the host material is often a particularly slow process, and can be further limited by other factors, including the structural response of the host material during ion insertion and diffusion. For many bulk battery materials, ion insertion requires a first-order phase transition, in which lithium ions are accommodated by forming a new phase, typically with expanded lattice parameters, though a nucleation-and-growth-type mechanism [8]. This process can require a high activation energy, so it tends to be slow, and limits ion insertion until its completion [8]. Alternatively, ion insertion in certain materials is accompanied by a second-order phase transition, or solid-solution-type mechanism, where Li is accommodated without forming a new phase, and the material's structure evolves continuously between lithiated and delithiated states. In this process, the lack of a discrete nucleation event to form another phase means that the activation energy and mechanical stress associated with the structure change tend to be much lower.

One common strategy to improve the rate capability of battery materials is to use nanostructured morphologies of the active electrode material instead of dense micron-scale particles [9,10]. This approach can dramatically shorten the distance needed for lithium to diffuse in the solid host particles. Additionally, the smaller crystal domain sizes in nanostructured materials can alter the mechanism for phase transformations driven by ion insertion [11]. Together, these effects can dramatically improve the charging kinetics of battery electrodes, but the specific details of how nanoscale crystal size affects phase transitions remain largely anecdotal for most materials, and there is a need for a mechanistic understanding that can aid the design of future fast-charging battery materials [9].

One aspect of ion insertion that has received relatively little interest is the role of ion ordering. Within the lattice of a host material, the interstitial sites where ions diffuse and reside form an interconnected sublattice, and even when the physical structure of an electrode is not changing, the mobile inserted ions can interact within this sublattice. At particular filling fractions within the host, the ions may form ordered arrangements corresponding to energetic minima [12]. Extensive theoretical and some experimental work has identified ion-ordered states in layered materials like graphite [13,14], Li_xTiS_2 [15,16] and $LiCoO_2$ [17], and these effects are broadly accepted as a key component for the thermodynamics of ion insertion in these materials [13,18]. However, there is less understanding of ion ordering in tunnel structured compounds, which are becoming more commonly used as electrode materials. For example, the best known tunnel structure material, lithium iron phosphate, does not appear to show ion ordering, while others, like some Wadsley-Roth structures, show clear, but relatively small, signatures of ordering [19,20].

Additionally, there is further need to understand the connection between ion ordering, structural dynamics, and ion insertion kinetics for electrode materials broadly [21]. Here, we examine the thermodynamics of lithium-ion insertion into MoO_2, a potential anode material for fast-charging lithium-ion batteries that has a rutile-type tunnel structure [22]. While micron-scale MoO_2 shows relatively slow kinetics, nanostructured morphologies of MoO_2 are much faster [23–27]. Recently, we demonstrated that bulk MoO_2's first order phase transitions, and the associated limitations on kinetics, are a major reason for its slowed charge storage [28]. For nanoscale MoO_2, however, these transitions become partially or fully suppressed, depending on the crystal size, which contributes to much faster cycling kinetics [28].

In this study, we use electrochemical thermodynamics analyses to connect the phase transition behavior of MoO_2 with ion ordering effects. First, we demonstrate that micron-scale MoO_2 stores lithium ions in three separate events, despite a single site for Li in its crystal structure, due to ion ordering. Notably, the largest ion ordering event coincides with the onset of the first-order phase transition and a local maximum in the measured overpotentials, which indicates that ion ordering likely drives the need for the phase transition, and that together these events slow charge storage significantly. Next, we find that in nanoscale MoO_2, with partially or completely suppressed phase transformations, that the signatures of ion ordering, and the related overpotential, are partially or almost completely suppressed, respectively. Finally, using *operando* calorimetry, we measured the heat generation of electrodes made with the different morphologies of MoO_2 during high rate cycling and found dramatic decreases in heat generation for the nanostructured materials. Overall, this work highlights the fundamental connection between ion ordering and phase transformation behavior and shows that the use of nanostructured materials can lead to relaxation of these phenomena and their negative influence on cycling kinetics.

2. Materials and methods

2.1. Materials

The following materials were obtained from commercial suppliers and used without further purification: ammonium molybdate (para) tetrahydrate $(NH_4)_6Mo_7O_{24}{\cdot}4H_2O$ (99%, Alfa Aesar), ammonium persulfate (98%, Alfa Aesar), ammonium lauryl sulfate (30% in water, Sigma Aldrich), molybdenum (V) chloride (99.6%, Alfa Aesar), methyl methacrylate (contains $\leq$ 30 ppm MEHQ as inhibitor, 99%, Sigma Aldrich).

2.2. Preparation of bulk and nanoporous MoO_2

The bulk and nanoporous MoO_2 samples were synthesized through a modified sol-gel route using freeze-drying. In this process, an aqueous solution of dissolved Mo precursor was frozen in liquid N_2 and dried under vacuum, then subsequently calcined to crystallize the material. To produce the nanoporous MoO_2, 150 - 200 nm polymer colloids were mixed with the initial solution of Mo precursor in order to template the nanoscale architecture.

Specifically, to synthesize bulk MoO_2, 200 mg of $(NH_4)_6Mo_7O_{24}{\cdot}4H_2O$ was added to 3 mL of water, then heated at 60 °C until it was fully dissolved. The resulting solution was frozen by dropwise addition into liquid N_2 and lyophilized on a Schlenk line with a pressure $<$ 200 mtorr for 12 to 24 h. The dried Mo precursor powder was then calcined in a quartz boat for 1 hour at 625 °C in flowing 5%H_2/95%N_2 with a 1-hour heating ramp and natural cooling rate.

For the synthesis of nanoporous MoO_2, a similar procedure was followed with slight modifications. First, 200 mg of $(NH_4)_6Mo_7O_{24}{\cdot}4H_2O$ was added to 2 mL of water, then heated at 60 °C until it was fully dissolved. Then, 2 to 4 mL of PMMA polymer colloid solution was added (depending on the density of colloids in solution) to obtain a 1:1 mass ratio of Mo precursor:colloid. The synthesis of the PMMA colloid solution is described below. After the Mo precursor-polymer colloid solution was mixed thoroughly, it was frozen by dropwise addition to liquid N_2 and lyophilized on a Schlenk line with a pressure $<$ 200 mtorr for 12 to 24 h. The dried Mo precursor polymer composite powder was calcined in a quartz boat in flowing Ar in two separate heating steps, with the powder cooled, removed from the furnace and exposed to air in between: first, at 550 °C for 1 hour, and then at 675 °C for 1 hour using a 1-hour heat ramp for each step and natural cooling rate. This two-heating-step process was employed to separate removal of the polymer templates from crystallization of the MoO_2 material. Since calcination occurs under anaerobic conditions, the polymer templates do not combust fully and, with a single heating step process, Mo carbides would form at the temperatures needed to crystallize the nanoporous MoO_2. After the second calcination, nanoporous MoO_2 samples were stored in inert atmosphere to avoid ambient oxidation.

2.3. Synthesis of poly(methyl methacrylate)(PMMA) colloid solution

The synthesis of PMMA colloids was adapted from a previous procedure described by Wang et al. [29]. For the nanoporous MoO_2 in this study, 150 - 200 nm colloids were used. Ammonium persulfate (APS)

was used as the initiator and ammonium lauryl sulfate (ALS) as the surfactant. APS, ALS, and deionized water were put into a three-neck round-bottom flask (250 mL) equipped with a magnetic stirrer, a reflux condenser, and a thermometer. After the temperature was raised to 75 °C, the monomer methyl methacrylate (MMA) was added. After monomer addition, the reaction temperature was kept at 80–85 °C for 1 hour before cooling. The concentrations of reagents were varied to make different sizes of PMMA. The as-synthesized PMMA colloidal aqueous solutions were extracted with hexane to remove excess monomer. Before use, the mass density of colloids in solution was measured by thermogravimetric analysis.

2.4. Synthesis of MoO_2 nanocrystals

MoO_2 nanocrystals were synthesized in a hydrothermal autoclave according to previously reported method with minor adaptations [27]. In a typical synthesis, 270 mg of $MoCl_5$, 15 mL of water, and 5 mL of ethanol were added to a 50 mL Teflon-lined Parr autoclave. The autoclave was sealed and heated for 6 h at 180 °C, then allowed to cool overnight. The product was centrifuged washed with ethanol three times. After the final wash, the powder was dried at 80 °C under vacuum. The as-synthesized nanocrystals were stored under inert atmosphere to prevent ambient oxidation.

2.5. Structural characterization

Scanning electron microscopy (SEM) images were obtained using a model JEOL JSM-6700F field emission electron microscope with 5 kV accelerating voltage and 6 mm working distance. Sample purity was assessed using laboratory X-ray diffraction collected with a PANalytical X'Pert Pro diffractometer operating with Cu Kα ($\lambda = 1.5418$ Å) using a 0.05 ° step size, an accelerating voltage of 45 kV, and a current of 40 mA.

2.6. Electrode and device fabrication

All MoO_2 powders were assembled into composite slurry electrodes for electrochemical testing. Electrodes had an overall composition of 70% active material, 10% multiwalled carbon nanotubes, 10% vapor-grown carbon fibers, and 10% polyvinylidene fluoride (PVDF) binder. Prior to preparing the slurry, the dry slurry components and current collector were heated at 100 °C under vacuum overnight. Then, the active material was ground dry with the carbon materials in a mortar and pestle. A PVDF binder solution (2.5%wt in N-methyl pyrrolidone) was added and mixed to produce a homogeneous paste that was cast onto an aluminum current collector with a doctor blade. The electrodes were dried under vacuum at 100 °C overnight. Electrodes with 0.7 mm diameter were punched out for electrochemical testing with mass loadings of active material of 1 – 1.5 mg/cm^2.

All electrochemical measurements were conducted in stainless-steel 2032 coin cells (MTI) with a stainless-steel conical spring, two 0.5-mm stainless-steel spacers, a 200 μm thick glass microfiber separator (Whatman), and a polished Li metal electrode (Sigma Aldrich). The electrolyte was 1 M $LiPF_6$ in 1:1 ethylene carbonate (EC): dimethyl carbonate (DMC), with 50 μL of electrolyte used per cell. All cycling experiments were performed between 1.1 V and 3 V vs. Li/Li$^+$on a VMP-300 potentiostat/galvanostat (BioLogic). When calculating C-rates, the theoretical capacity C_{theo} was taken as 210 mAh/g, based on 1 electron Li$^+$insertion reaction into MoO_2 (1C = 210 mA/g, and 5C = 1.05 A/g.).

2.7. Operando synchrotron X-ray diffraction (SXRD)

Operando SXRD was conducted at beamline 11–3 at the Stanford Synchrotron Radiation Lightsource at 12.7 keV, using modified coin cells with Be spacers, as adapted from Chien et al. [30]. While conventional modified coin cells use stainless steel spacers with holes to provide X-ray transparency, experiments done with these cells are susceptible to artifacts due to the lack of stack pressure and electrical conductivity in the region probed by the X-ray beam. Our improved cell design uses Be spacers, which do not have holes, and thus remain both rigid and conductive to accurately recreate the cycling environment in a typical coin cell. Beryllium metal discs 15 mm in diameter and 0.5-mm thick were purchased from American Elements (99%). Caution: Beryllium oxide particulates formed from machining or breaking beryllium are carcinogenic and the material should be handled with caution.

2.8. Potentiometric entropy measurements

The open-circuit voltage $U_{OCV}(x,T)$ and entropic potential $\partial U_{OCV}(x,T)/\partial T$ of the half coin cells with MoO_2 electrodes made of bulk, nanoporous, or nanocrystals were measured as functions of lithium composition x at 20 °C using the procedure and apparatus described in Ref [31]. The galvanostatic intermittent titration technique (GITT) was performed with 30-minutes pulses at C/10. Those were followed by a ~ 270 min relaxation periods during which the temperature was changed in 5 °C increments between 15 °C and 25 °C in the last 40 min. The cell potential was measured with a high accuracy potentiostat (BioLogic, VSP-300). To confirm the cell was in thermodynamic equilibrium, the following conditions had to be satisfied: (i) the temperature difference between the cold plate and the top of the coin cell was <0.1 °C and (ii) the time rate of change of the open-circuit voltage $\partial U_{OCV}/\partial t$ was <1 mV/h. The lithium composition in Li_xMoO_2 was estimated as

$$x = \frac{C}{MC_{theo}} \tag{1}$$

where C is the measured capacity (in mAh), M is the mass loading of active material (in g), and C_{theo} is the theoretical capacity of MoO_2 (= 210 mAh/g).

From a thermodynamics standpoint, the open-circuit voltage $U_{OCV}(x,T)$ of a battery cell made of MoO_2 particles with a lithium counter electrode can be expressed as [32].

$$U_{OCV}(x,T) = -\frac{\mu_{Li_xMoO_2}(x,T) - \mu^{\circ}_{Li}(T)}{e} \tag{2}$$

where e is the elementary charge while $\mu_{Li_xMoO_2}(x,T)$ and $\mu^{\circ}_{Li}(T)$ are the chemical potential of Li_xMoO_2 and metallic lithium, respectively. Because the temperature derivative of the Gibbs free energy is the entropy, the entropy analogue to the chemical potential, termed the entropic potential, is given by $\partial U_{OCV}(x,T)/\partial T$, and is defined as [32]

$$\frac{\partial U_{OCV}(x,T)}{\partial T} = \frac{1}{e}\left[\frac{\partial s_{Li_xMoO_2}(x,T)}{\partial x} - s^{\circ}_{Li}(T)\right] \tag{3}$$

where $s_{Li_xMoO_2}(x,T)$ is the molar entropy of the Li_xMoO_2 electrode which depends on x. By contrast, the standard molar entropy of lithium $s^{\circ}_{Li}(T)$ is independent of x. Potentiometric entropy measurements obtain the entropic potential $\partial U_{OCV}(x,T)/\partial T$ of a battery cell as a function of lithium composition x for given pressure and temperature. These measurements help gain insight into the physicochemical phenomena occurring in battery electrodes during cycling. In other words, U_{OCV} and $\partial U_{OCV}(x,T)/\partial T$ capture changes in the fundamental thermodynamics properties of redox active materials. Thus, analyzing $U_{OCV}(x,T)$ and $\partial U_{OCV}(x,T)/\partial T$ can identify physicochemical phenomena occurring during lithiation and delithiation of MoO_2 such as intercalation in via a solid-solution mechanism, two-phase coexistence [19,32]and ion ordering [32].

2.9. Operando isothermal calorimetry

Operando isothermal calorimetry was performed on each cell with the different MoO_2 electrodes using the apparatus described in Ref [33]. The cells consisted of a 1 cm × 1 cm MoO_2 working electrode and a 1 cm

× 1 cm metallic lithium counter electrode immersed in 1 M $LiPF_6$ in 1:1 EC:DMC. The cells were tested under galvanostatic cycling using a high accuracy potentiostat (BioLogic, SP-150). Simultaneously, the instantaneous heat generation rates at each electrode were measured based on the heat fluxes $q_i''(t)$ (in mW/cm^2) measured using 1 cm × 1 cm thermoelectric heat flux sensors (greenTEG, gSKIN-XP) placed behind each electrode such that

$$\dot{Q}_i(t) = q_i''(t)A_i = \frac{\Delta V_i(t)}{S_i}A_i \; with \; i = MoO_2 \; or \; Li \tag{4}$$

where A_i (in cm^2) is the area of the heat flux sensor and electrode, $\Delta V_i(t)$ (in μV) is the voltage difference measured by the heat flux sensor, and S_i is the sensitivity of the heat flux sensor (in μV/(W/cm^2)). The total instantaneous heat generation rate is the sum of both $\dot{Q}_{MoO_2}$ and $\dot{Q}_{Li}$ i.e., $\dot{Q}_T(t) = \dot{Q}_{MoO_2}(t) + \dot{Q}_{Li}(t)$. The instantaneous heat generation rate at electrode "i" can also be divided into a reversible and an irreversible contribution, i.e., $\dot{Q}_i(t) = \dot{Q}_{irr,i}(t) + \dot{Q}_{rev,i}(t)$. In order to minimize the white noise in the measured signal, the measured heat generation rates were averaged over the last three cycles of period t_{cd} for each imposed current, i.e.,

$$\dot{Q}_i(t) = \frac{1}{3}\sum_{j=1}^{3}\dot{Q}_i[t + (j-1)t_{cd}]. \tag{5}$$

Finally, the net electrical energy losses ΔE_e (in J) over one cycle is the difference between the electrical energy input and output. Graphically, ΔE_e is the area enclosed by the hysteric voltage $V(x,T)$ vs. the charge transferred q. and is expressed as [34]

$$\Delta E_e = \oint_{cycle} V(x,T)dq = \oint_{cycle} V(x,T)Idt. \tag{6}$$

Similarly, the thermal energy dissipated during a cycle can be defined as [34]

$$Q_T = \oint_{cycle} \dot{Q}_T(t) \tag{7}$$

Following the first law of thermodynamics, the net electrical energy loss is equal to the total thermal energy dissipated during one cycle, i.e., $\Delta E_e = Q_T$. In order to account for the difference of capacity across the different types of MoO_2, both the net electrical energy loss and the thermal energy were divided by the capacity C_m.

3. Thermodynamic modeling

Baek et al. [32]developed a simple thermodynamic model for ion ordering under solid-solution type intercalation considering Li ions intercalating in two sublattices with different site energies (ϵ_1 and ϵ_2) and no interaction between the guest cations. The model was able to capture the effects of ion ordering on the open-circuit voltage $U_{OCV}(x,T)$ and entropic potential $\partial U_{OCV}(x,T)/\partial T$ as a function of Li composition x for materials that show solid-solution type insertion, two-phase coexistence, and first-order phase transitions.

In the present study, this model was modified to consider three sublattices each with different site energies, namely ϵ_1, ϵ_2, and ϵ_3, with $\epsilon_1 < \epsilon_2 < \epsilon_3$. Then, the Gibbs free energy of the system $g_{Li_xMoO_2}(x,T)$ can be expressed as [32]

$$g_{Li_xMoO_2}(x,T) = g_{MoO_2}(T) + \epsilon_1 x_1 + \epsilon_2 x_2 + \epsilon_3 x_3 - Ts_{Li_xMoO_2}(x,T)$$

where $g_{MoO_2}(x,T)$ is the Gibbs free energy of the host MoO_2, $s_{Li_xMoO_2}(x,T)$ is the entropy of the Li_xMoO_2 electrode, while x_1, x_2 and x_3 correspond to the local concentrations of Li ions in each sublattice. Further expressing the entropy $s_{Li_xMoO_2}(x,T)$ as the ideal solution configurational entropy, the free energy of an ideal intercalation compound with three sublattices can be expressed as [32]

$$\begin{aligned} g_{Li_xMoO_2}(x,T) = {} & g_{MoO_2}(T) + \epsilon_1 x_1 + \epsilon_2 x_2 + \epsilon_3 x_3 \\ & + k_B T[x_1 \ln x_1 + (1-x_1)\ln(1-x_1)] \\ & + k_B T[x_2 \ln x_2 + (1-x_2)\ln(1-x_2)] \\ & + k_B T[x_3 \ln x_3 + (1-x_3)\ln(1-x_3)] \end{aligned} \tag{8}$$

For the sake of simplicity, in the current model, all sublattices were assumed to be the same size, but in general, the only requirement is that i.e., $x = (x_1 + x_2 + x_3)$, with x being the total Li composition in Li_xMoO_2. For any increment in x, the model numerically computed the combination of x_1, x_2 and x_3 that minimizes the Gibbs free energy $g_{Li_xMoO_2}(x,T)$. Then, the open-circuit voltage of a cell made of a Li_xMoO_2 electrode with metallic Li as the counter electrode can be written as [32]

$$U_{OCV}(x,T) = -\frac{1}{e}\left[\frac{\partial g_{Li_xMoO_2}(x,T)}{\partial x} - \mu_{Li}^{\circ}(T)\right] \tag{9}$$

where $\mu_{Li}^{\circ}(T)$ is the chemical potential of the metallic Li. The entropic potential of the cell is expressed as [32]

$$\frac{\partial U_{OCV}(x,T)}{\partial T} = \frac{1}{e}\left[\frac{\partial s_{Li_xMoO_2}(x,T)}{\partial x} - s_{Li}^{\circ}(T)\right] \tag{10}$$

with $s_{Li}^{\circ}(T)$, the entropy of metallic lithium reported to be 29 J/mol·K. The values of ϵ_1, ϵ_2 and ϵ_3 were selected arbitrarily to replicate qualitatively the trends observed in the potentiometric entropy measurements, with Cases A, B, and C, corresponding to electrodes with bulk and nanoporous MoO_2 particles, and MoO_2 nanocrystals, respectively. The absolute and relative values of ϵ_1, ϵ_2 and ϵ_3 (around 0.1 - 1 eV) were similar to those obtained from DFT calculations for Li_xCoO_2 [35]and $Li_xPNb_9O_{25}$ [20]which both exhibit ion ordering upon lithiation.

4. Results and discussion

In this study, we employed micron-scale bulk MoO_2, nanoporous MoO_2, and MoO_2 nanocrystal powders as a model system for understanding how phase transition behavior affects electrochemical performance. The synthesis and detailed characterization of these materials, as well as the full characterization of their phase transition behavior during cycling were recently reported [28]. Both the nanoporous MoO_2 and MoO_2 have nanoscale crystallites, with the nanocrystals having smaller crystallites on average based on Scherrer analysis of X-ray diffraction data.

4.1. Size-controlled MoO_2 as a model system for phase transition behavior

Fig. 1(a)–(c) show the scanning electron microscopy (SEM) images of bulk, nanoporous and nanocrystal MoO_2 powders. The bulk MoO_2 particles were anisotropic and approximately 1 – 10 μm in diameter [Fig. 1(a)]. The nanoporous MoO_2 consisted of micron-scale particles with ~150 nm pores throughout the material [Fig. 1(b)]. Finally, the MoO_2 nanocrystals comprised of individual particles 15 – 30 nm in diameter loosely agglomerated into larger secondary particles [Fig. 1(c)].

MoO_2 is often studied for its high capacity conversion reaction in which it is fully reduced to form Mo metal and Li_2O. However, this reaction suffers from large volume change and the formation of insulating regions of Li_2O, which hinder its reversibility and rate capability. Here, we limited the lower voltage bound to 1.1 V vs. Li/Li$^+$to access the one electron insertion reaction in which Li$^+$is reversibly (de)inserted into vacant interstitial sites within the tunnels of MoO_2. This reaction has a moderate theoretical capacity of 210 mAh/g but shows significantly improved cyclability and scalability compared to the conversion

$$MoO_2 + xe^- + xLi^+ \rightleftharpoons Li_xMoO_2 (0 \le x \le 1) \tag{11}$$

Fig. 2(a) reports the galvanostatic rate capability of electrodes made

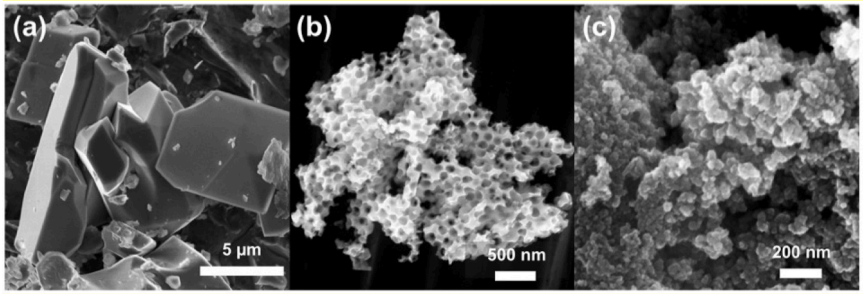

Fig. 1. Scanning electron microscopy (SEM) characterization of (a) bulk MoO_2, (b) nanoporous MoO_2, and (c) MoO_2 nanocrystals.

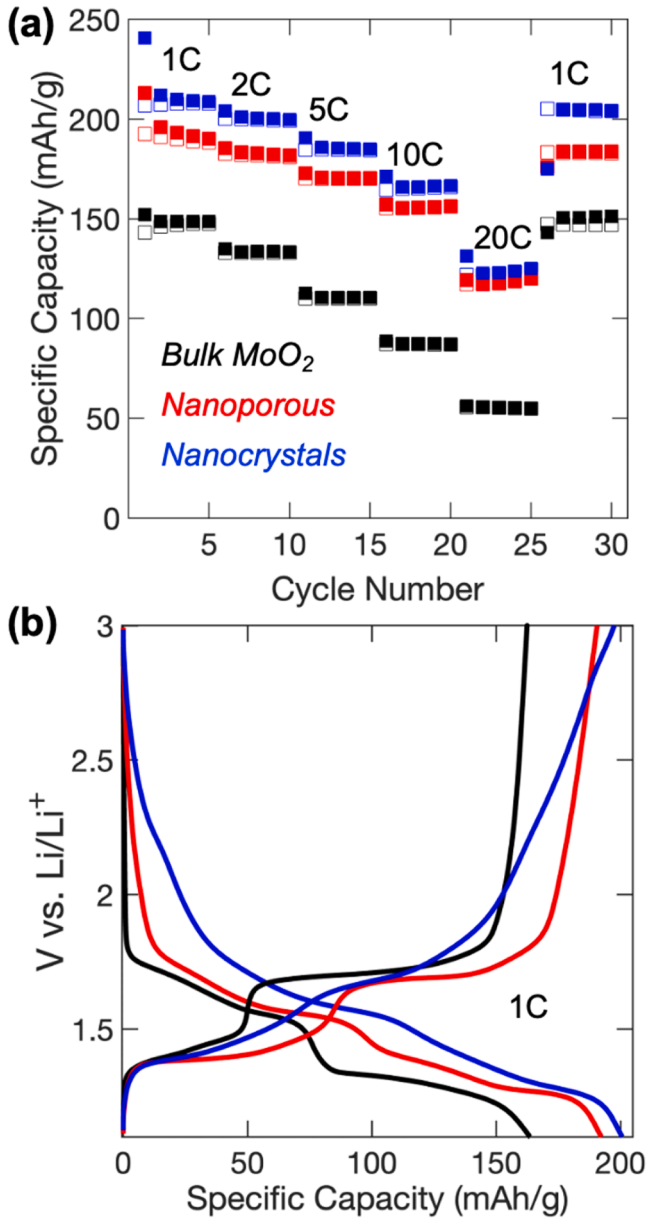

Fig. 2. (a) Galvanostatic rate testing and (b) galvanostatic profile for the different MoO_2 samples. Bulk MoO_2 shows low capacity and poor retention at high rates, while both nanostructured materials show strong capacity and rate capability.

with the three representative MoO_2 materials at C-rates ranging from 1C to 20C. Electrodes made of nanoporous MoO_2 and MoO_2 nanocrystals showed excellent cycling performance with near completion of the insertion reaction at slow rates, and strong retention of capacity at faster rates. Bulk MoO_2, on the other hand, could only store about 150 mAh/g at 1C, and retained a third of that capacity at 20C. The galvanostatic charge storage profiles of the three materials also showed key differences with clear plateaus for bulk MoO_2 replaced by sloping profiles to different extents in the nanoscale MoO_2 [Fig. 2(b)].

The structural change of the MoO_2 powders during cycling were characterized using *operando* X-ray diffraction, with the most intense (011) reflection highlighted for clarity in Fig. 3(a)–(c). Each material began as pristine unlithiated MoO_2 and finished lithiation with the same $LiMoO_2$ phase. However, the pathway between these two states varied for each type of MoO_2. Halfway through the lithiation, bulk MoO_2 microparticles featured a first-order phase transition with a large miscibility gap, followed by another first-order phase transition near the end of lithiation that did not complete due to the voltage cutoff. In the same regions, nanoporous MoO_2 particles again featured a first-order phase transition, but the miscibility gap was smaller and the composition span of the two-phase coexistence region was dramatically shorter. Finally, for the MoO_2 nanocrystals, the entire lithiation process occurred as a continuous solid-solution process. As such, these MoO_2 materials provide a model system for comparing materials with the same basic redox reaction for charge storage, but three distinct types of phase transformation behavior.

4.2. Linking ion ordering to structural dynamics and kinetic overpotentials

Fig. 4 shows (a,b) the open-circuit voltage $U_{OCV}(x)$, (c,d) the entropic potential $\partial U_{OCV}(x)/\partial T$, (e,f) the overpotential $\eta(x) = V(x) - U_{OCV}(x)$ during GITT measurements at C/10 and $T = 20\,^{\circ}C$, and (g,h) the unit cell volume during constant current lithiation and delithiation at C/5 as a function of lithium composition for bulk MoO_2 electrodes. The overpotential $\eta(x)$ is defined as the difference between the open-circuit voltage $U_{OCV}(x)$ and the closed-circuit voltage $V(x)$ at the end of the current pulse. It is a direct measure of the additional electrode polarization required to drive the charge storage process at a given state-of-charge. A large overpotential indicates kinetically slow charge storage processes in a given composition range. Since GITT takes place under quasi-equilibrium conditions, under which ion and electron transport should not be kinetically limited, the measured overpotential is especially sensitive to kinetic barriers that are intrinsic to charge storage within the electrode material itself. Note also that the refined lattice parameters and unit cell volume were obtained from a separate *operando* SXRD experiment. In that experiment, the bulk MoO_2 electrode was cycled at C/5, not under GITT conditions. To enable comparison to the GITT data, the galvanostatic profiles were adjusted to account for the additional overpotential and a slightly different composition range. Comparison between the original and adjusted data is shown in Figure S1.

Both lithiation and delithiation processes were divided into four different regions, based on the four different redox peaks of MoO_2

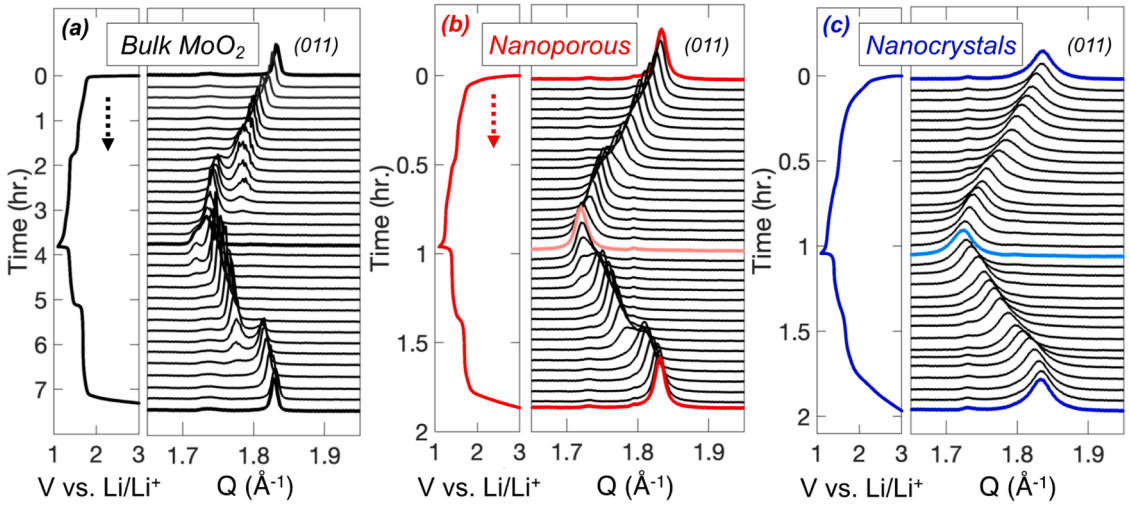

Fig. 3. Operando SXRD of the MoO_2 materials. (a) Bulk MoO_2 undergoes large first-order phase transitions during lithium insertion, while (b) nanoporous MoO_2 shows phase transitions that are still first-order, but with a decreased lattice miscibility gap and duration of two-phase coexistence. (c) MoO_2 nanocrystals do not have a first-order phase transition at all, and instead exhibit a second-order-type solid-solution insertion process.

identified in Ref [28]. The regions are identified in the dQ/dV plot shown in Supplementary Material (Figure S2). The fact that the peaks in the dQ/dV align across all electrodes made of MoO_2 enables a more relevant comparison of the three electrodes. In Region I, defined by $0 \leq x < 0.18$, the open-circuit voltage $U_{OCV}(x)$ and the entropic potential $\partial U_{OCV}(x)/\partial T$ of the bulk MoO_2 electrode decreased monotonically while the unit cell volume increased linearly. The overpotential was low, indicating relatively facile charge storage in Region I. This behavior indicated lithium intercalation in a solid-solution manner [19,36,37].

In Region II ($0.18 \leq x < 0.47$), the open-circuit voltage U_{OCV} continued decreasing but with a much smaller slope compared to Region I, indicating larger capacity per voltage step, as also observed in the corresponding dQ/dV plots (Figure S2). At the start of Region II, the entropic potential $\partial U_{OCV}(x)/\partial T$ displayed a tilde shape fluctuation. The behavior of $U_{OCV}(x)$ and $\partial U_{OCV}(x)/\partial T$ is characteristic of formation of an ion-ordered state in a material that otherwise shows solid-solution behavior, as discussed in detail in Reference [32]. In brief, the ion-ordered state results in a local minimum in $\partial U_{OCV}(x)/\partial T$ and a sharp increase immediately after, as ions begin to be inserted into the next site. After the first ion ordering signature in bulk MoO_2, more lithium was inserted in Region II, and the overpotential increased sharply, reaching a maximum at the end of Region II. These events coincide with the onset of a first-order phase transition, shown by the appearance of a new set of lattice parameters in the unit cell volume data at the start of Region III ($0.47 \leq x < 0.77$). Lithium insertion proceeded in Region III, during the coexistence of the two phases. The phase transition resulted in a sharp drop in the overpotential η while the open-circuit voltage exhibited another inflection, and the entropic potential exhibited a second tilde fluctuation at the boundary between Regions II and III. Combined, these observations indicate a second instance of ion ordering in bulk MoO_2 particles during lithiation. Moreover, this second ion ordering immediately preceded the first-order phase transformation, observed in the unit cell volume for $x \geq 0.5$. Usually, two-phase coexistence is associated with both constant open-circuit voltage and constant entropic potential, as in lithium iron phosphate, for which both the lithium-rich and lithium-poor phases maintain the same lattice parameters throughout the phase transformation [32]. However, here the entropic potential shows a clear tilde shape, centered on the phase-transition point. This tilde is consistent with the structural evolution that occurs during the bulk MoO_2 phase transition, which involves solid-solution changes in the lattice parameters until the first-order transition, which then appears as a discontinuity in the lattice parameters and the entropic potential. After the transition (and the associated increase in entropic potential), the solid-solution evolution continues with decreasing entropic potential.

In Region IV ($0.77 \leq x < 0.89$), around the end of the lithiation process - associated with the fourth redox peak around 1.4 V - the open-circuit voltage plateaued and the entropic potential decreased. From the cyclic voltammogram of Ref [28], the fourth peak showed large capacity at this potential. In addition, the SXRD data [Fig. 4(g)]indicates that Region IV corresponds to the second first-order phase transformation that did not complete due to the cutoff voltage, explaining the plateau in the open-circuit voltage. Minimal change in the entropic potential is observed in this region, but the small decrease could potentially be explained by the increase in unit cell volume of the second phase during the two-phase coexistence.

Overall, these results suggest that the structural evolution of bulk MoO_2 is intricately linked to the mechanism of ion insertion. In particular, the largest signature of ion ordering occurred at the onset of a first-order phase transition. This link between the two events suggests that the ion-ordered state represents an energetic minimum that is deep enough that an entirely new phase must be formed for ion insertion to proceed. Importantly, these processes coincided with a clear maximum in the measured overpotential, which indicates that they slow charge storage considerably.

During delithiation, bulk MoO_2 showed largely similar behavior to that observed during lithiation, with a few notable differences. The open-circuit voltage curve featured two plateaus in Regions IV ($0.87 \geq x > 0.63$) and II ($0.48 \geq x > 0.23$), and a very large tilde in the entropic potential is observed at the junction between Region III ($0.63 \geq x > 0.48$) and Region II. As with lithiation, the same ion ordering event at $x \sim 0.48$ coincided with the onset of a first-order phase transition, shown by a new set of lattice parameters. However, one key difference compared to lithiation was that the overpotential was dramatically smaller during this event. Instead of the large spike in overpotential of up to nearly 200 mV shown at the onset of the phase transition during lithiation, the phase transition was accompanied by only a small local increase of 65 mV during delithiation. This observation indicates that the phase transition during delithiation is kinetically more facile than during lithiation. This discrepancy may result from mechanistic differences in the phase progression, which is different for delithiation than for lithiation, even though the end phases are the same. Because both phase transitions are driven by the same ion ordering event, the unit cell volume data in Fig. 4 shows two-phase coexistence over very different stoichiometries: across Region III ($0.47 \leq x < 0.77$) for lithiation, and across Region II ($0.48 \geq x > 0.23$) on delithiation. The difference can be

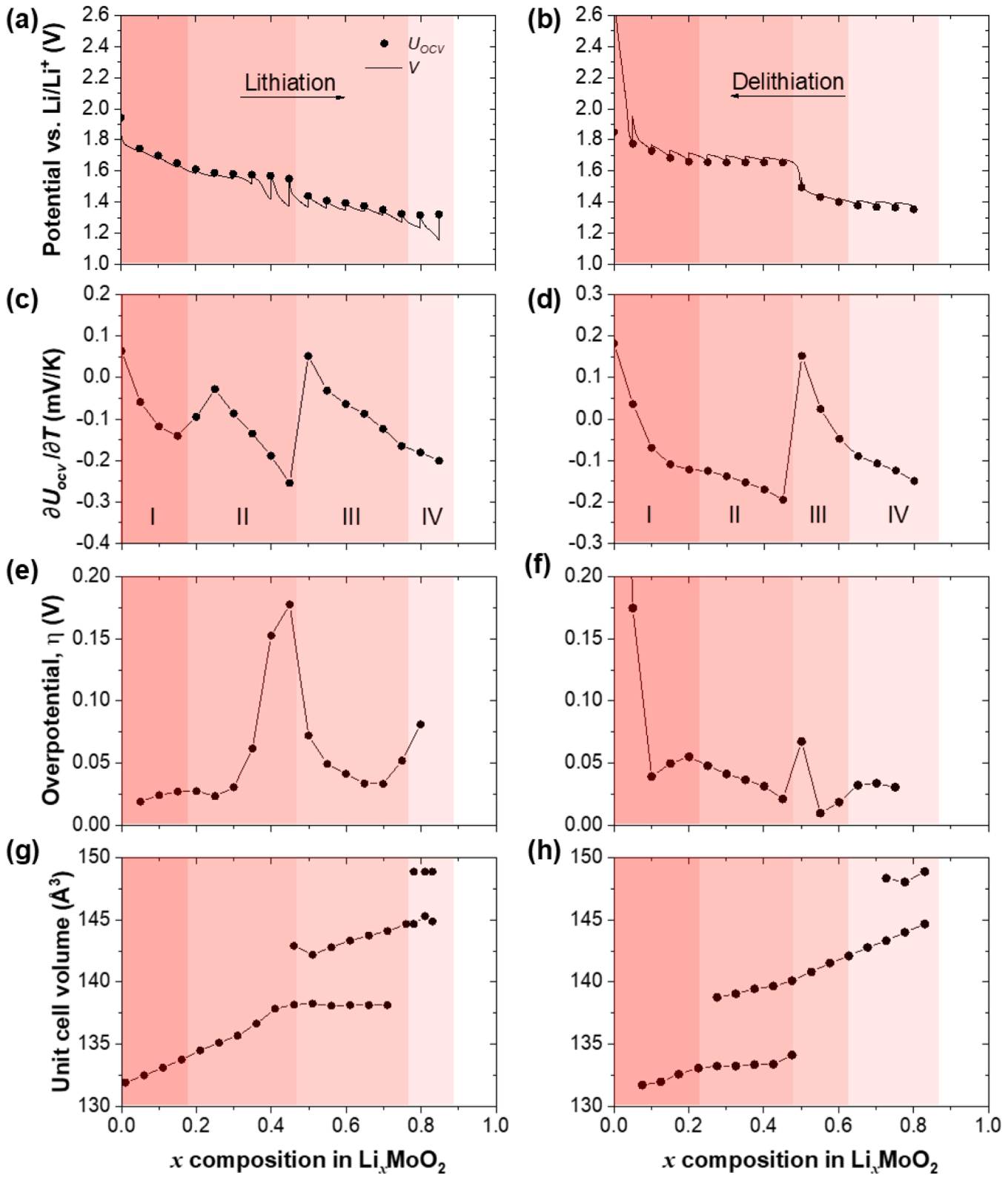

Fig. 4. Experimental measurements on bulk MoO_2 of (a,b) open-circuit voltage $U_{OCV}(x)$, (c,d) entropic potential $\partial U_{OCV}(x)/\partial T$, (e,f) overpotential $\eta(x) = V(x) - U_{OCV}(x)$ as functions of lithium composition x during GITT at C/10 and $T = 20$ °C, and (g,h) lattice parameters from *operando* SXRD. The *operando* SXRD is from a separate cycling experiment with the composition x-axis adjusted based on the galvanostatic profile.

attributed to the large ion ordering event occurs at approximately $x = 0.5$, and to the fact that the phase transformation follows immediately after, which supports our hypothesis that the phase transformation occurs to move the system out of the ion ordered state. These findings point to a clear connection between the phase asymmetry of lithiation and delithiation and the presence of the ion ordering that may be relevant to understanding the phase behavior of other battery materials.

4.3. Nanoscale size can partially or completely disrupt ion ordering

With the connection between charge storage mechanism, ion ordering, and structural change established for bulk MoO_2, we now examine how nanoscale size affects these processes. Fig. 5 shows the same thermodynamic analysis as in Fig. 4 for the three types of MoO_2 electrodes investigated (i.e., bulk, nanoporous, and nanocrystals) as a function of lithium composition x. Additionally, several quantitative

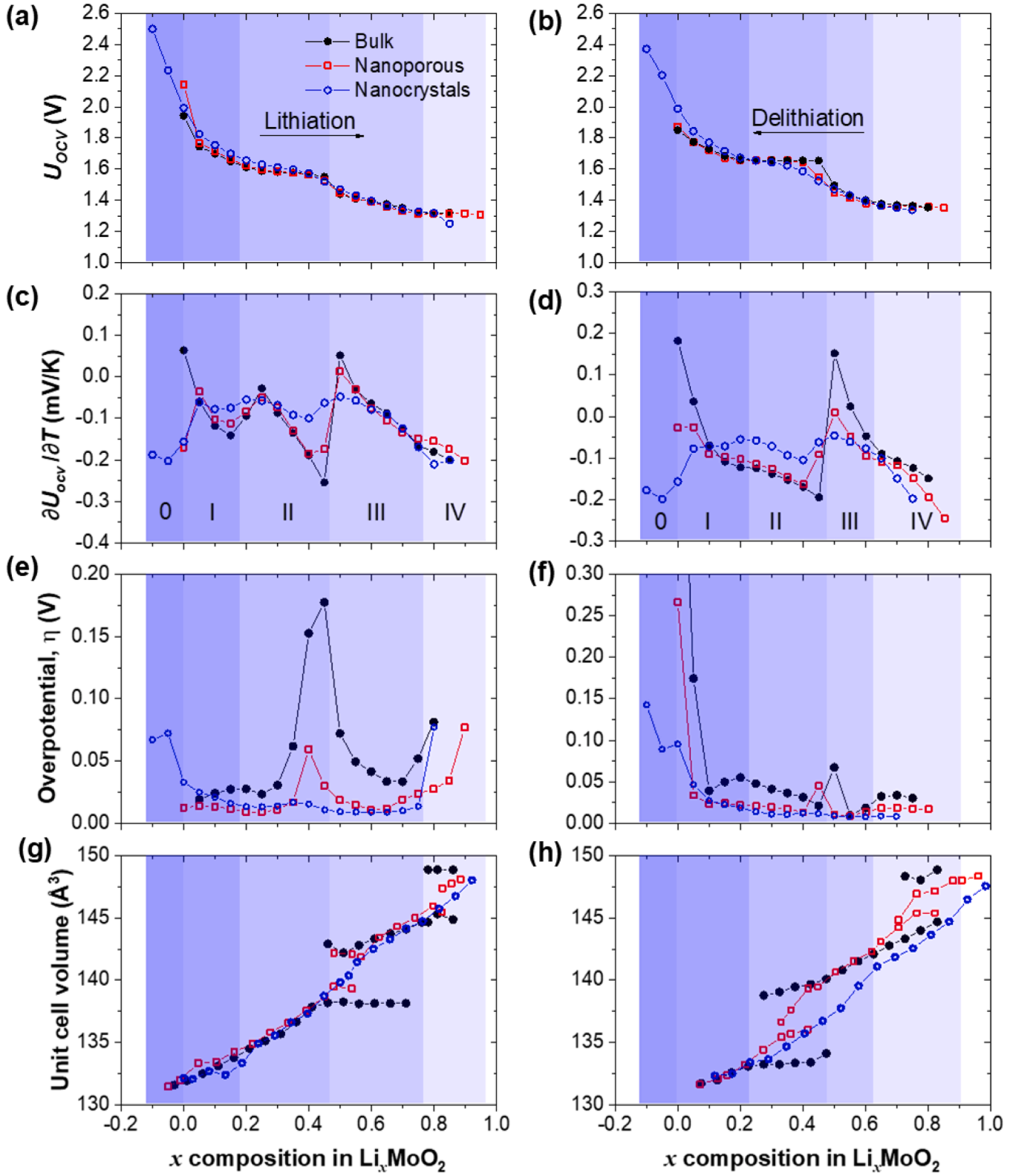

Fig. 5. Experimental measurements on the different MoO_2 materials of (a,b) open-circuit voltage $U_{OCV}(x)$, (c,d) entropic potential $\partial U_{OCV}(x)/\partial T$, (e,f) overpotential $\eta(x) = V(x) - U_{OCV}(x)$ as functions of lithium composition x during GITT at C/10 and 20 °C, and (g,h) lattice parameters from operando SXRD. The *operando* SXRD is from a separate cycling experiment with the composition x-axes adjusted based on the galvanostatic profiles.

parameters of interest extracted from the data are provided in Table 1. Note that the MoO_2 nanocrystals exhibited additional capacity at the beginning of the lithiation [shown above 2 V in the galvanostatic profile in Fig. 2(b)], which has been previously attributed to redox at under-coordinated surface sites. To account for this capacity and allow for better comparison of the primary charge storage processes among the three materials, we shifted the measured composition in the GITT data for the MoO_2 nanocrystals based on the amount of high voltage capacity from the under-coordinated surface redox, which corresponded to $x \sim 0.1$. Additionally, the unit cell volume data was adjusted slightly to account for the different overpotential in the operando SXRD experiment, with the original and adjusted data compared in Figures S3 and S4. The same four regions previously identified were defined across the three types of electrodes, with one additional region ($x < 0$) defined for the electrode made of MoO_2 nanocrystals. Fig. 5(a) indicates that the open-circuit voltage $U_{OCV}(x)$ of the electrodes made with nanoporous MoO_2 particles was similar to that of bulk MoO_2 but the plateau regions were more sloped. On the other hand, $U_{OCV}(x)$ obtained with MoO_2 nanocrystals had no discrete plateaus, and instead the entire profile is sloping. As discussed previously, the largest ion ordering event, the onset of the primary first-order phase transition, and the maximum overpotential occurred simultaneously for bulk MoO_2, at the boundary between Regions II and III. These features were also observed for the intermediate size nanoporous MoO_2, albeit with smaller magnitudes. For example, the magnitude of the largest tilde in the entropic potential $\partial U_{OCV}(x)/\partial T$, which indicates the extent of ion ordering, in the nanoporous MoO_2 electrode (0.19 mV/K) was less than two-thirds that observed for bulk MoO_2 (0.31 mV/K), as measured by the peak-to-peak difference in the $\partial U_{OCV}(x)/\partial T$.

The two-phase coexistence Region III also showed a smaller mismatch in lattice parameters and unit cell volume (4.7 $Å^3$ for bulk vs. 2.7 $Å^3$ for nanoporous) between the two coexisting phases and a narrower composition range. With less pronounced ion ordering and a smaller phase transition, the associated overpotentials were much smaller, with a local maximum of 60 mV around $x = 0.47$ compared to 180 mV for bulk MoO_2. This smaller overpotential indicates that the disruption of the ion ordering and/or the partial suppression of the phase transformation considerably decreased the kinetic limitations ion insertion over this composition range. Importantly, the effects observed with nanoporous MoO_2 particles were even more pronounced for the smaller sized MoO_2 nanocrystals. At the transition between Regions II and III, the MoO_2 nanocrystals showed almost no signature of ion ordering at all (0.04 mV/K), and did not show a first-order phase transition. In fact, the unit cell volume evolved continuously and proceeded through lithium insertion in a solid-solution manner. Accordingly, the overpotential remained small (20 mV) and nearly constant.

Similar changes to the charge storage mechanism were also observed during delithiation. At the transition between Regions III and II, the large ion ordering event, which showed a fluctuation δ_{deriv} of 0.35 mV/K for bulk MoO_2, was diminished for nanoporous MoO_2 (0.17 mV/K), and nearly gone for the nanocrystals (0.04 mV/K), and the associated overpotentials decreased accordingly. As noted previously, the overpotential at the phase transition was much lower for bulk MoO_2 during delithiation than during lithiation (65 mV vs. 180 mV), indicating a more facile delithiation process. In agreement with this trend, the local maximum overpotential η_{max} notably decreased to 46 mV and 9 mV in the nanoporous and nanocrystal materials, respectively, which indicated a meaningful change in kinetics in the finite sized materials.

Overall, these results establish that the absence of ion ordering in MoO_2 nanocrystals coincided with the suppression of the first-order phase transition. The relaxation of the ion ordering and the concurrent suppression of the phase transformation seen here has not been previously demonstrated, and emphasizes the interconnected roles of ion ordering and structural dynamics during charge storage. An open question remaining is the specific structural cause of the changed phase behavior and ion ordering among the three different MoO_2 materials. The crystallite size is one obvious difference, as the greater contribution of surface energies to the total free energy of nanoscale crystallites could affect the thermodynamics of ion insertion. Another likely candidate is the defect density within the crystal structure, which typically decreases with higher synthesis temperature. Both the bulk and nanoporous MoO_2 were synthesized at high temperature (>500 °C), while the MoO_2 nanocrystals were synthesized hydrothermally (180 °C), and the discrepancy likely contributes to the more dramatic change in behavior seen for the nanocrystals. Additional work is necessary to quantify which of these structural components is the primary cause of the altered ion ordering and phase transformation behavior in the MoO_2 nanocrystals.

Table 1
Input parameters to the three-site thermodynamic model for the three different cases.

Case	ϵ_1 (eV)	ϵ_2 (eV)	ϵ_3 (eV)	Corresponding Material
A	0.38	0.42	0.48	Bulk MoO_2
B	0.38	0.415	0.465	Nanoporous MoO_2
C	0.38	0.41	0.445	Nanocrystals MoO_2

4.4. Modeling of ion ordering in 3 sites

To complement the previous experimental results for the three different types of electrodes simulations of the open-circuit voltage and entropic potential profiles were performed using the three-site thermodynamic model introduced in the Methods section. Here, the relative energy difference between the ion ordering sites were varied to reproduce qualitatively the observations of Fig. 5(a)–(d) and further explain the effects of particle size.

Fig. 6 shows the model predictions for (a) the sublattice differential site filling $\partial x_i/\partial x$ ($1 \leq i \leq 3$), (b) the entropy $s_{Li_xMoO_2}(x)$, (c) the open-circuit voltage $U_{OCV}(x)$, and (d) the entropic potential $\partial U_{OCV}(x,T)/\partial T$ at $T = 20$ °C during lithiation of the modeled battery cell as a function of lithium composition x for the three arbitrary cases A, B, and C with different values of ϵ_1, ϵ_2 and ϵ_3 listed in Table 2. Fig. 6 also reproduces measurements of (e) the open-circuit voltage $U_{OCV}(x)$ and (f) the entropic potential $\partial U_{OCV}(x)/\partial T$ for the three types of electrodes as a function of lithium composition x during lithiation. The model predictions were divided into three regions of equal size associated with the successive filling of the three sublattices by increasing site energy ϵ_1, ϵ_2 and ϵ_3. In Region I ($0 \leq x < 0.33$), sublattice 1 was filled almost exclusively. The entropy of the working electrode $s_{Li_xMoO_2}$ increased and the entropic potential $\partial U_{OCV}(x)/\partial T$ decreased. As x approached 0.18, sublattice 1 was half full and its contribution to entropy started to decrease as the differential site filling $\partial x_1/\partial x$ started decreasing while $\partial x_2/\partial x$ increased. Between $x = 0.25$ and $x = 0.45$, both sublattices 1 and 2 were filled, and at $x = 0.33$, $\partial x_2/\partial x > \partial x_1/\partial x$, as it became energetically more favorable to fill sublattice 2 than sublattice 1. Then, the entropy $s_{Li_xMoO_2}$ increased again leading to a tilde fluctuation in $\partial U_{OCV}(x,T)/\partial T$ [Fig. 6(c)]. Simultaneously, $U_{OCV}(x)$ featured a slight step at $x = 0.33$. Eventually, sublattice 1 became full, and sublattice 2 was filled almost exclusively, corresponding to Region II ($0.33 \leq x < 0.66$). At $x = 0.5$, sublattice 2 became half full, and its entropy contribution started to decrease. As $x \geq 0.6$, $\partial x_2/\partial x$ decreased and $\partial x_3/\partial x$ increased sharply, and became larger than $\partial x_2/\partial x$ at $x = 0.66$, causing a step in U_{OCV}, an increase in entropy $s_{Li_xMoO_2}$, and a second tilde fluctuation in $\partial U_{OCV}(x)/\partial T$.

Note that for all three cases, the range of x during which sublattice 2 and 3 were filled was shorter than when sublattice 1 and 2 were being filled. This was due to the fact that the difference $\Delta\epsilon_{23} = \epsilon_3 - \epsilon_2$ was larger than $\Delta\epsilon_{12} = \epsilon_2 - \epsilon_1$. Indeed, following Eq. (8), as $\Delta\epsilon$ increased, it became energetically favorable to fill almost exclusively the lower energy sublattice before the higher energy one. $\Delta\epsilon_{12}$ and $\Delta\epsilon_{23}$ were the

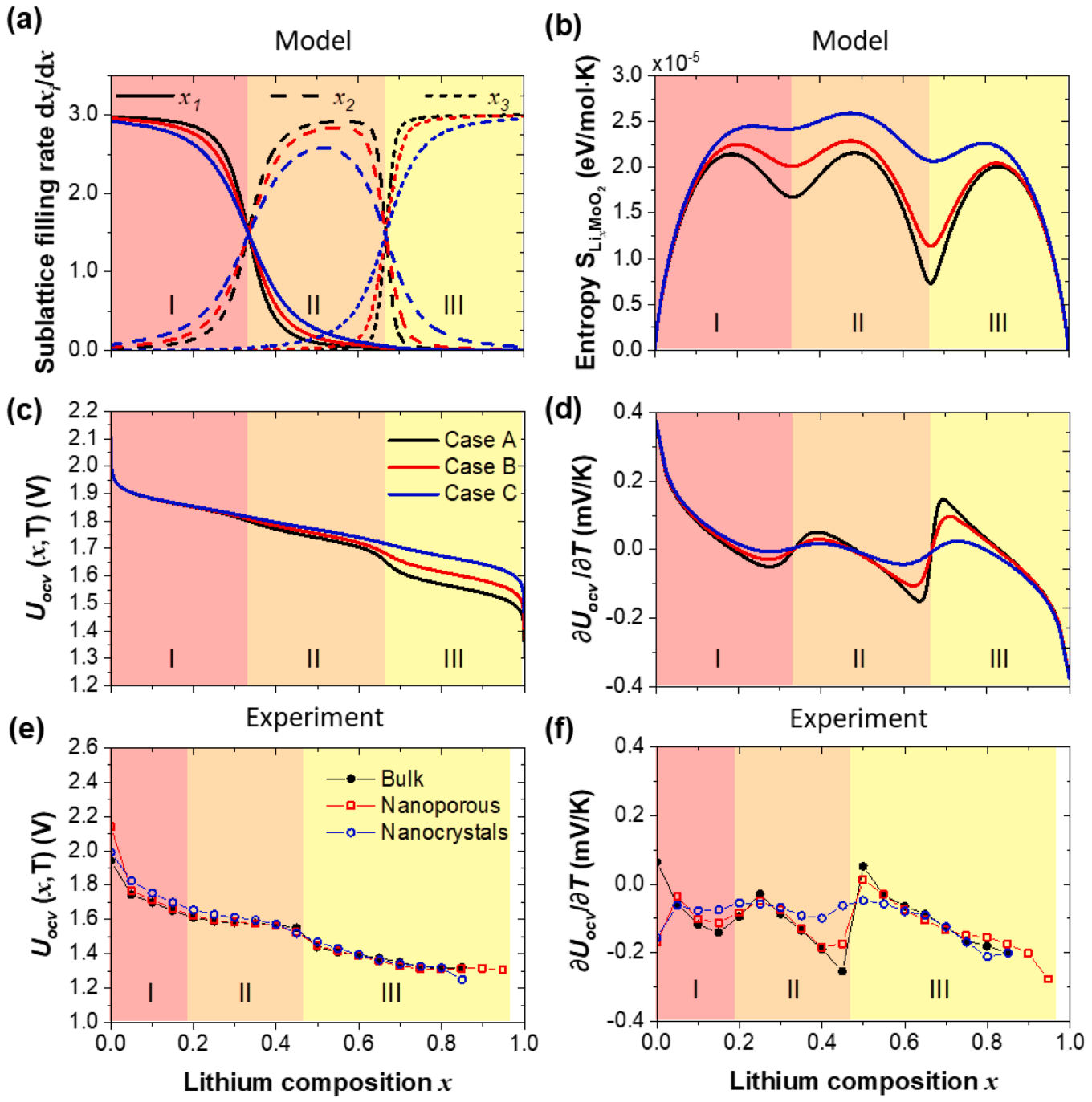

Fig. 6. Model predictions for the (a) sublattice differential site filling $\partial x_i/\partial x1 \leq i \leq 3$, (b) entropy $s_{Li_xMoO_2}(x)$, (c) open-circuit voltage $U_{OCV}(x)$, and (d) entropic potential $\partial U_{OCV}(x)/\partial T$ of the modeled battery cell as functions of lithium composition x for Cases A-C listed of Table 1. Experimental measurements of (e) open-circuit voltage $U_{OCV}(x)$, (f) entropic potential $\partial U_{OCV}(x)/\partial T$ on electrodes made of different types of MoO_2 particles.

Table 2
Quantitative parameters extracted from the thermodynamic analysis for the three MoO_2 materials during lithiation and delithiation.

Parameter	Definition	Units	Bulk		Nanoporous		Nanocrystals	
			Lith.	Delith.	Lith.	Delith.	Lith.	Delith.
U_{OCV}	OCV at onset of the main ion-ordering event	V	1.55	1.49	1.53	1.45	1.52	1.52
δ_{deriv}	Extent of entropic potential fluctuation around the ion-ordered state	mV/K	0.31	0.35	0.19	0.17	0.04	0.04
η_{max}	Local maximum in overpotential	mV	180	65	60	46	20	9
ΔV	Miscibility gap during phase transition	Å^3	4.7	6.0	2.7	3.3	N/A	N/A

largest for Case A (corresponding to bulk MoO_2), and smallest for Case C (corresponding to MoO_2 nanocrystals). The range of x during which two sublattices were filled concurrently can be considered as an ion ordering region. As this range of x became shorter, the dips in entropy became

deeper, and the tilde fluctuations in the entropic potential became sharper. In Case A, two significant dips were observed in the open-circuit voltage $U_{OCV}(x)$, at the transitions at $x = 0.33$ and 0.66, with the second dip larger than the first one. These dips became smaller for Case B, and almost negligible for Case C, as $\Delta\epsilon_{12}$ and $\Delta\epsilon_{23}$ became smaller.

Overall, the model predictions displayed similar magnitudes and dips in the open-circuit voltage U_{OCV}, and tilde fluctuation in the entropic potential $\partial U_{OCV}(x,T)/\partial T$ as those observed experimentally [Fig. 6(e) and 6(f)]. Here also, for every electrode, the first tilde was smaller than the second one, indicating a larger energy difference between the second and third sites compared to the first and second sites. These results provide support for the mechanism of strong ion ordering observed in bulk MoO_2 that is partly relaxed in the nanoporous MoO_2, and nearly completely relaxed in the MoO_2 nanocrystals. Additionally, the model indicates that these effects could be driven by the relative differences in site energies ϵ_i $(1 \leq i \leq 3)$ associated with the three ion sublattices.

4.5. *Effect of nanosizing on hysteresis*

During constant current galvanostatic cycling or cyclic voltammetry experiments, hysteresis between charge and discharge at high rates is commonly used to assess kinetic performance. In a GITT experiment, however, the cell is under very slow, quasi-equilibrium cycling conditions when lithium diffusion and electron transport should not be limiting factors. Under these conditions, little hysteresis would be expected, except for intrinsically slow processes, so observations of hysteresis with GITT can provide insight into the fundamental charge

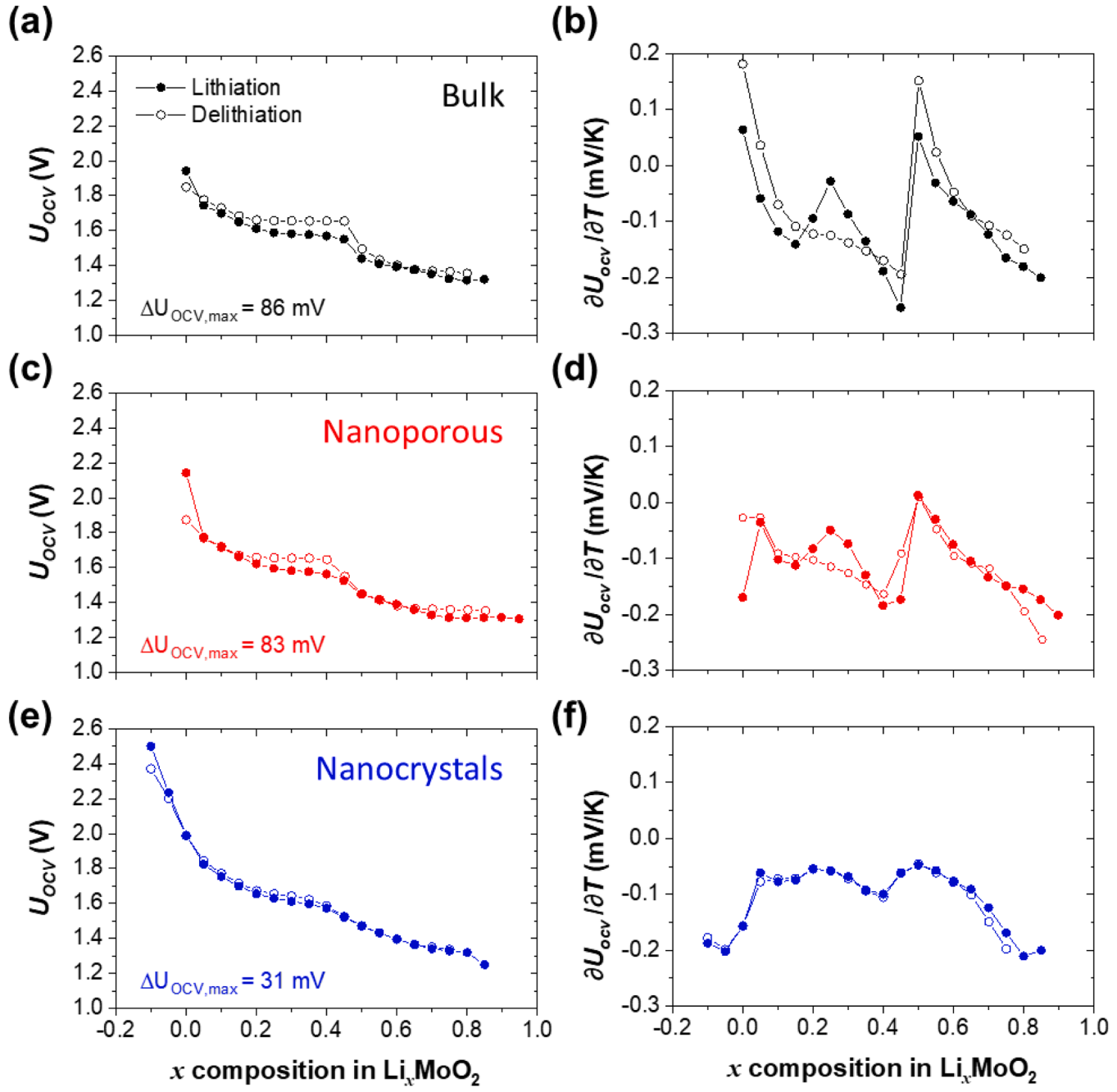

Fig. 7. Hysteresis under quasi-equilibrium GITT conditions between lithiation and delithiation in experimentally measured open-circuit voltage $U_{OCV}(x)$and entropic potential $\partial U_{OCV}(x)/\partial T$ for electrodes made of (a,b) bulk MoO_2 or (c,d) nanoporous MoO_2 nanoparticles, and (e,f) MoO_2 nanocrystals.

storage mechanism. Accordingly, we examined the hysteresis between lithiation and delithiation in the open-circuit voltage $U_{OCV}(x)$ and entropic potential $\partial U_{OCV}(x)/\partial T$ as measured by GITT. Despite the very slow cycling conditions for the measurements, clear hysteresis was apparent between lithiation and delithiation in $U_{OCV}(x)$ and $\partial U_{OCV}(x)/\partial T$ for electrodes made from bulk MoO_2 [Fig. 7(a) and (b)]. The difference in the open-circuit voltage varies across the composition range, with the largest gap of 86 mV occurring in the two-phase coexistence regions during phase transformations. Likewise, electrodes made of nanoporous MoO_2 particles showed two regions with significant hysteresis corresponding also to first-order phase transitions, with a maximum hysteresis of 83 mV [Fig. 7(c) and (d)]. However, electrodes made of MoO_2 nanocrystals did not have any first-order phase transition and instead their lattice evolution during cycling occurred entirely through a second-order solid-solution-type process [Fig. 7(e) and (f)]. Accordingly, the hysteresis observed with bulk and nanoporous MoO_2 particles was almost nonexistent for the MoO_2 nanocrystals, with a maximum of 31 mV. This notable difference indicates that hysteresis between lithiation and delithiation occurs as a result of the ion ordering event and the related first-order phase transitions, even at very low cycling rates. Notably, despite the much lower kinetic overpotentials of nanoporous MoO_2 compared to bulk (60 mV versus 180 mV on lithiation), the hysteresis in $U_{OCV}(x)$ remained similar. In contrast, the MoO_2 nanocrystals, which showed near-complete relaxation of the ion ordering and suppression of the first-order phase transition, exhibited very little hysteresis in $U_{OCV}(x)$. These results emphasize the key connection between ion ordering, the phase transformation behavior, and hysteresis in $U_{OCV}(x)$ during cycling. For the entropic potential, lithiation and delithiation are largely similar. The size of the largest tilde and its occurrence at $x \sim 0.5$ are about the same for lithiation and delithiation, which supports that the hysteresis in $U_{OCV}(x)$ is driven by the ordering. One notable discrepancy, though, is the absence of a second tilde on delithiation for the bulk and nanoporous MoO_2, which indicates that the secondary ion ordering does not occur on delithiation.

4.6. Heat generation rate during cycling with operando calorimetry

Finally, we used *operando* isothermal calorimetry to evaluate the effect of the differences in the thermodynamics of ion insertion and transport phenomena in the three different type of MoO_2 materials considered. Fig. 8 shows the instantaneous heat generation rates measured at electrodes made of bulk and nanoporous MoO_2 particles and MoO_2 nanocrystals, as well as at the corresponding Li metal counter electrode as a function of dimensionless cycling time t/t_{cd}, where t_{cd} is the charge and discharge time, for 1C, 2C, and 3C. Here, the first half of the cycle corresponds to delithiation and the second half to lithiation. For all C-rates, the heat generation rate at the bulk MoO_2 electrode was the largest, while it was the lowest at electrodes made from MoO_2 nanocrystals. Notably, the heat generation rate of the nanoporous MoO_2 varied throughout cycling. At the beginning of delithiation, for example, the heat generation was relatively high (similar to heat generation in bulk MoO_2), while by the end of delithiation, it was much lower and closer to that of the MoO_2 nanocrystals. For all samples, the heat generation rate was positive throughout delithiation, while the beginning of lithiation had a slightly negative heat generation rate that increased during the cycle.

In general, the heat generation during cycling occurs from a combination of resistive Joule heating, reversible entropy changes, and irreversible heat of mixing. Joule heating results when electrode kinetics limit the acceptance of current and result in overpotential, while the entropy changes result from reversible chemical reactions occurring within the electrode. All kinetic effects contribute to irreversible heat generation including ion transport (which is affected by surface area and electrode porosity), and the overpotential from phase behavior. Reversible heat generation is affected by the thermodynamics of the phase behavior. It is difficult to fully separate these effects, and all likely contribute to the lower heat generation observed for the nanostructured materials. The nanoporous MoO_2 and MoO_2 nanocrystals, for example, have much better charge storage kinetics both from more facile ion transport and from decreased overpotential due to phase behavior. These effects were reflected in the calorimetry data with lower heat generation in the nanostructured materials. Additionally, the dramatic changes in phase behavior for both the nanostructured materials, but especially the nanocrystals, would likely alter the thermodynamics of the phase behavior and thereby lower the heat generation.

Fig. 9 shows the specific net electrical energy losses $\Delta E_e/C_m$ [Eq. (6)] and the specific total thermal energy dissipated Q_T/C_m [Eq. (7)], measured independently over a charging/discharging cycle for calorimetric cells with working electrodes made of bulk and nanoporous MoO_2 particles, and MoO_2 nanocrystals. For all electrodes, the net electrical energy losses $\Delta E_e/C_m$ increased with increasing current, as expected. At all currents, the electrode made of bulk MoO_2 particles had the largest electrical energy losses, consistent with its worse kinetics. Conversely, the MoO_2 nanocrystals electrode had the lowest energy losses, even at 3C. These results reaffirm the improved performance and decreased energy loss as a result of the faster charge storage dynamics in the nanostructured materials, especially in the MoO_2 nanocrystals. Finally, for all cells and at all C-rates, the total heat generation Q_T/C_m measured during *operando* isothermal calorimetry fell within the experimental uncertainty ($\sim$ 10%) of the net electrical energy loss $\Delta E_e/C_m$ measured independently. These results confirm that all electrical energy losses were dissipated as heat.

5. Conclusion

In this study, we used potentiometric entropy measurements to demonstrate the presence of ion ordering in electrodes of Li_xMoO_2, a potential fast-charging anode material. The signatures of ion ordering coincided with key events in the material's structural dynamics, which we probed with *operando* SXRD. In bulk MoO_2 particles, ion ordering coincided with the onset of a first-order phase transition, which establishes a link between the presence of an ion-ordered energetic minimum and the need for a phase-transformation. Additionally, a large overpotential was measured during these processes, indicating that ion ordering slowed charge storage considerably. In nanostructured versions of MoO_2 particles, the ion ordering, phase transitions, and overpotentials were partially or completely suppressed, depending on the crystal size. For intermediate size nanoporous MoO_2 particles, the indicators of ion ordering were present, but with smaller magnitude than in bulk MoO_2. Accordingly, nanoporous MoO_2 shows a phase transition that is still first-order, but with smaller lattice mismatch, shorter two-phase coexistence region, and lower overpotential. In even smaller MoO_2 nanocrystals, the ion ordering disappeared nearly completely, the structural evolution was through Li insertion in a solid-solution manner, and the cell overpotential was small and constant. Finally, *operando* isothermal calorimetry showed that heat dissipation and electrical energy losses were the lowest in the electrode made of MoO_2 nanocrystals compared to those made with bulk and nanoporous MoO_2 particles as a result of both faster kinetics and different charge storage mechanism.

Overall, this work establishes a clear mechanistic link between ion ordering, structural dynamics and charge storage kinetics for Li_xMoO_2. While it is widely known that large structural changes during ion insertion can hinder the charge storage process, this connection to ion ordering provides potential new insight into why phase transformations occur in the first place. As such, this work provides guiding principles for the design and understanding of fast-charging electrode materials.

CRediT authorship contribution statement

Nicolas Leport: Writing – review & editing, Writing – original draft, Visualization, Validation, Resources, Methodology, Investigation, Formal analysis, Data curation, Conceptualization. **Daniel D.**

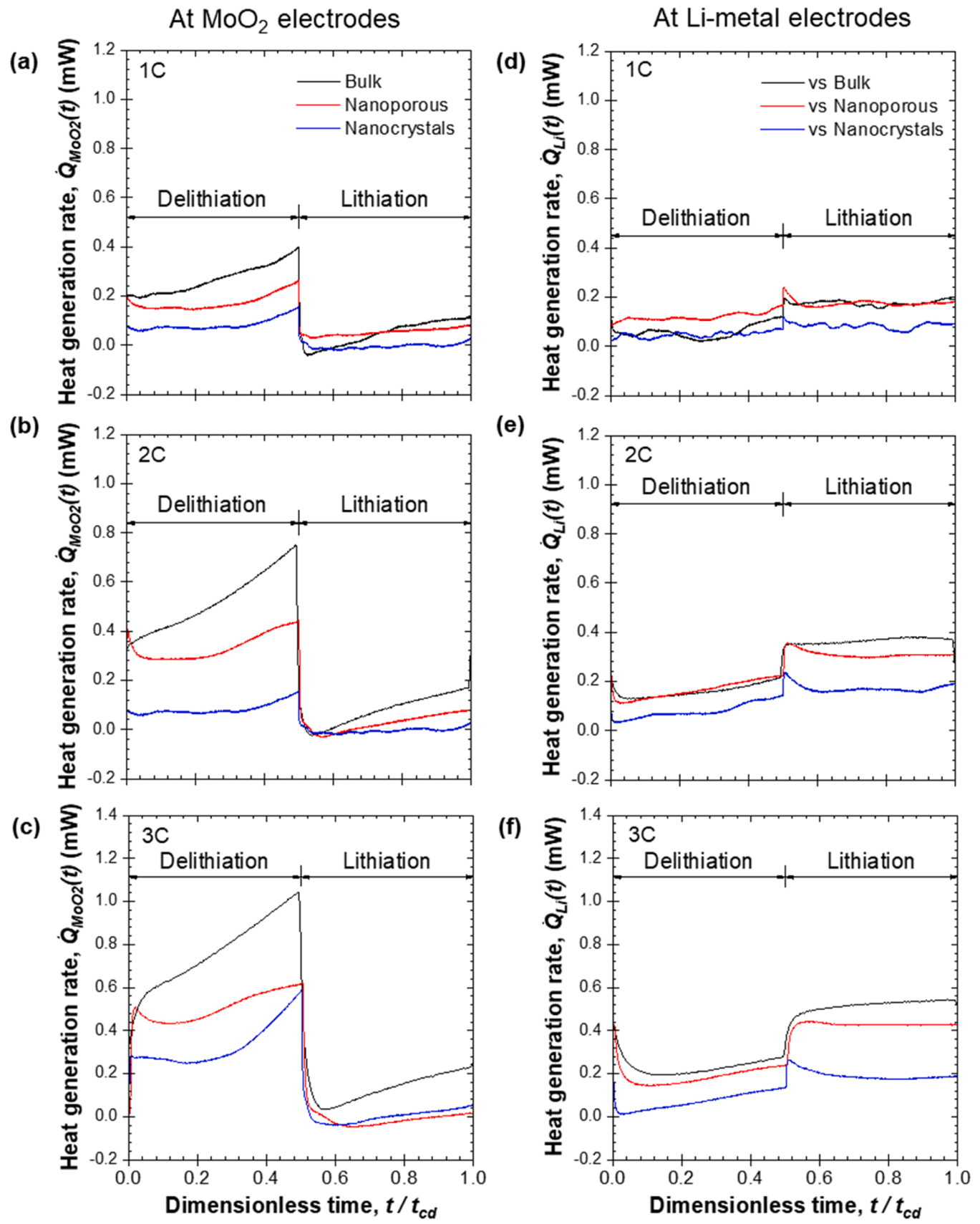

Fig. 8. (a,b,c) Instantaneous heat generation rate $\dot{Q}_{MoO_2}(t)$ at working electrode made of bulk and nanoporous MoO_2 particles, and MoO_2 nanocrystals, and (d,e,f) $\dot{Q}_{Li}(t)$ at the lithium metal electrodes for the same three cells, all as functions of dimensionless time t/t_{cd} at (a,d) 1C, (b,e) 2C, and (c,f) 3C.

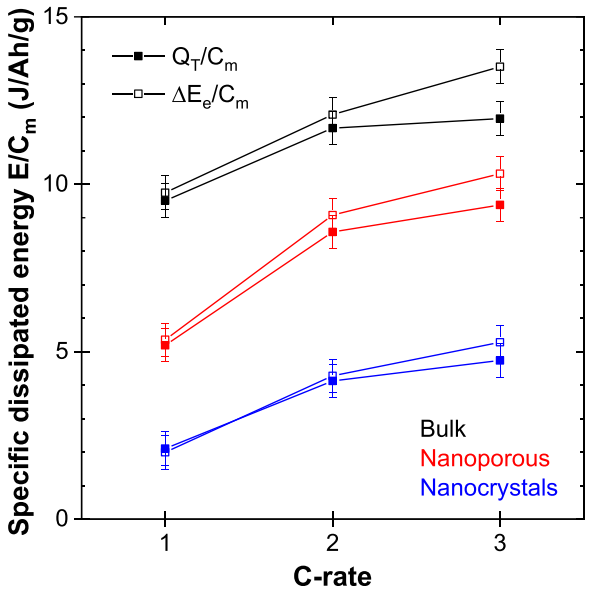

Fig. 9. Net specific electrical energy loss $\Delta E_e/C_m$ and total specific thermal energy dissipated Q_T/C_m over a charging/discharging cycle for calorimetric cells with working electrodes made of bulk and nanoporous MoO_2 particles, and MoO_2 nanocrystals.

Robertson: Writing – review & editing, Writing – original draft, Visualization, Validation, Resources, Methodology, Investigation, Formal analysis, Data curation, Conceptualization. **Yucheng Zhou:** Writing – original draft, Resources, Methodology, Investigation, Formal analysis, Data curation. **Sarah H. Tolbert:** Writing – review & editing, Supervision, Project administration, Investigation, Funding acquisition, Conceptualization. **Laurent Pilon:** Writing – review & editing, Supervision, Resources, Project administration, Methodology, Investigation, Funding acquisition, Conceptualization.

Declaration of competing interest

The authors declare that they have no known competing financial interests or personal relationships that could have appeared to influence the work reported in this paper.

Acknowledgements

This work was supported by the US Department of Energy, Office of Basic Energy Sciences. Primary support came from Award DE-SC0014213. D.D.R. acknowledges support from a National Science Foundation Graduate Research Fellowship under award DGE-2034835. XRD experiments were conducted at beamline 11–3 of the Stanford Synchrotron Radiation Lightsource (SLAC National Accelerator Laboratory). The authors thank Dr. Molleigh Preefer and Dr. Kevin Stone for user support. Use of the Stanford Synchrotron Radiation Lightsource, SLAC National Accelerator Laboratory, is supported by the U.S. Department of Energy, Office of Science, Office of Basic Energy Sciences under Contract No DE-AC02-76SF00515. This research used resources of the Advanced Photon Source, a U.S. Department of Energy (DOE) Office of Science User Facility operated for the DOE Office of Science by Argonne National Laboratory under Contract No DE-AC02-06CH11357. Operando XRD of bulk MoO_2 was performed at beamline 11-ID-C. The authors thank Kamila Wiaderek for user support.

Supplementary materials

Supplementary material associated with this article can be found, in the online version, at doi:10.1016/j.ensm.2026.105224.

Data availability

Data will be made available on request.

References

[1] V. Zinth, C. Von Lüders, M. Hofmann, J. Hattendorff, I. Buchberger, S. Erhard, J. Rebelo-Kornmeier, A. Jossen, R. Gilles, Lithium plating in lithium-ion batteries at sub-ambient temperatures investigated by in situ neutron diffraction, J. Power. Sources 271 (2014) 152–159.
[2] M.B. Preefer, M. Saber, Q. Wei, N.H. Bashian, J.D. Bocarsly, W. Zhang, G. Lee, J. Milam-Guerrero, E.S. Howard, R.C. Vincent, Multielectron redox and insulator-to-metal transition upon lithium insertion in the fast-charging, Wadsley-Roth phase PNb$_9$O$_{25}$, Chem. Mater. 32 (2020) 4553–4563.
[3] K.J. Griffith, A.C. Forse, J.M. Griffin, C.P. Grey, High-rate intercalation without nanostructuring in metastable Nb2O5 bronze phases, J. Am. Chem. Soc 138 (28) (2016) 8888–8899.
[4] H. Liu, Z. Zhu, Q. Yan, S. Yu, X. He, Y. Chen, R. Zhang, L. Ma, T. Liu, M. Li, R. Lin, A disordered rock salt anode for fast-charging lithium-ion batteries, Nature 585 (7823) (2020) 63–67.
[5] D.D. Robertson, C.Z. Salamat, D.J. Pe, H. Cumberbatch, D.N. Agyeman-Budu, J. Nelson Weker, S.H. Tolbert, Electrochemically-formed disordered rock salt ω-li$_x$v$_9$mo$_6$o$_{40}$ as a fast-charging Li-ion electrode material, Chem. Mater. 36 (24) (2024) 11770–11780.
[6] K.J. Griffith, K.M. Wiaderek, G. Cibin, L.E. Marbella, C.P. Grey, Niobium tungsten oxides for high-rate lithium-ion energy storage, Nature 559 (2018) 556–563.
[7] S. Li, K. Wang, G. Zhang, S. Li, Y. Xu, X. Zhang, X. Zhang, S. Zheng, X. Sun, Y. Ma, Fast charging anode materials for lithium-ion batteries: current status and perspectives, Adv. Funct. Mater. 32 (2022) 2200796.
[8] R. Malik, F. Zhou, G. Ceder, Kinetics of non-equilibrium lithium incorporation in LiFePO$_4$, Nat. Mater. 10 (2011) 587–590.
[9] Z. Song, W. Jiang, X. Jian, F. Hu, Advanced nanostructured materials for electrocatalysis in lithium–sulfur batteries, Nanomaterials 12 (2022) 4341.
[10] P.G. Bruce, B. Scrosati, J.-M. Tarascon, Nanomaterials for rechargeable lithium batteries, Angew. Chem. Int. Ed. 47 (2008) 2930–2946.
[11] W. Qi, J.G. Shapter, Q. Wu, T. Yin, G. Gao, D. Cui, Nanostructured anode materials for lithium-ion batteries: principle, recent progress and future perspectives, J. Mater. Chem. A 5 (2017) 19521–19540.
[12] A. Van der Ven, J. Bhattacharya, A.A. Belak, Understanding Li diffusion in Li-intercalation compounds, Acc. Chem. Res 46 (2013) 1216–1225.
[13] Y. Reynier, R. Yazami, B. Fultz, Thermodynamics of lithium intercalation into graphites and disordered carbons, J. Electrochem. Soc. 151 (3) (2004) A422.
[14] D. Allart, M. Montaru, H. Gualous, Model of lithium intercalation into graphite by potentiometric analysis with equilibrium and entropy change curves of graphite electrode, J. Electrochem. Soc. 165 (2018) A380.
[15] A. Thompson, Thermodynamics of Li intercalation batteries: entropy measurements on Li$_x$TiS$_2$, Phys. B C 105 (1–3) (1981) 461–465.
[16] J. Dahn, R. Haering, Entropy measurements on Li$_x$TiS$_2$, Can. J. Phys. 61 (7) (1983) 1093–1098.
[17] Y. Shao-Horn, F. Weill, L. Croguennec, D. Carlier, M. Ménétrier, C. Delmas, Lithium and vacancy ordering in T# 2- Li$_x$CoO$_2$ derived from O$_2$-type LiCoO$_2$, Chem. Mater. 15 (2003) 2977–2983.
[18] H. Kim, Y. Park, Y. Kwon, J. Shin, Y.-H. Kim, H.-S. Ahn, R. Yazami, J. Choi, Entropymetry for non-destructive structural analysis of LiCoO$_2$ cathodes, Energy Env. Sci 13 (1) (2020) 286–296.
[19] S.W. Baek, M.B. Preefer, M. Saber, K. Zhai, M. Frajnkovič, Y. Zhou, B.S. Dunn, A. Van der Ven, R. Seshadri, L. Pilon, Potentiometric entropy and calorimetric measurements reveal fast charging mechanisms in PNb$_9$O$_{25}$, J. Power. Sources. 520 (2022) 230776.
[20] M. Saber, M.B. Preefer, S.K. Kolli, W. Zhang, G. Laurita, B. Dunn, R. Seshadri, A. Van der Ven, Role of electronic structure in Li ordering and chemical strain in the fast charging Wadsley–Roth phase PNb$_9$O$_{25}$, Chem. Mater. 33 (2021) 7755–7766.
[21] M.S. Whittingham, Lithium batteries and cathode materials, Chem. Rev 104 (2004) 4271–4302.
[22] J.R. Dahn, W.R. McKinnon, Structure and electrochemistry of Li$_x$MoO$_2$, Solid State Ion. 23 (1987) 1–7.
[23] S. Hu, F. Yin, E. Uchaker, W. Chen, M. Zhang, J. Zhou, Y. Qi, G. Cao, Facile and green preparation for the formation of MoO$_2$-GO composites as anode material for lithium-ion batteries, J. Phys. Chem. C 118 (2014) 24890–24897.
[24] H. Wang, T. Li, A.M. Hashem, A.E. Abdel-Ghany, R.S. El-Tawil, H.M. Abuzeid, A. Coughlin, K. Chang, S. Zhang, H. El-Mounayri, Nanostructured molybdenum-oxide anodes for lithium-ion batteries: an outstanding increase in capacity, Nanomaterials 12 (2021) 13.
[25] Y. Yan, H.S. Kim, J.B. Cook, S. Robbennolt, B. Dunn, S.H. Tolbert, Mesoporous MoO$_2$ thin films for high rate Li+ storage: effect of crystallinity and porous structure, Solid State Sci. 129 (2022) 106890.
[26] Y. Yan, M.A. Chin, D.D. Robertson, B.K. Lesel, S.H. Tolbert, Tuning the porous structure in PMMA-templated mesoporous MoO$_2$ for pseudocapacitive Li-ion electrodes, J. Electrochem. Soc. 169 (2022) 040545.
[27] H.-S. Kim, J.B. Cook, S.H. Tolbert, B. Dunn, The development of pseudocapacitive properties in nanosized-MoO$_2$, J. Electrochem. Soc. 162 (2015) A5083–A5090.

[28] D.D. Robertson, H. Cumberbatch, D.J. Pe, Y. Yao, S.H. Tolbert, Understanding how the suppression of insertion-induced phase transitions leads to fast charging in nanoscale Li_xMoO_2, ACS Nano 18 (2024) 996–1012.
[29] T. Wang, O. Sel, I. Djerdj, B. Smarsly, Preparation of a large mesoporous CeO_2 with crystalline walls using PMMA colloidal crystal templates, Colloid. Polym. Sci. 285 (2006) 1–9.
[30] Y. Chien, A.S. Menon, W.R. Brant, M.J. Brandell, Simultaneous monitoring of crystalline active materials and resistance evolution in lithium–sulfur batteries, J. Am. Chem. Soc 142 (2020) 1449–1456.
[31] S.W. Baek, K.E. Wyckoff, D.M. Butts, J. Bienz, A. Likitchatchawankun, M. B. Preefer, M. Frajnkovič, B.S. Dunn, R. Seshadri, L. Pilon, Calorimetry informs the origin of rapid rate performance in microwave-prepared $TiNb_2O_7$ electrodes, J. Power Sources 490 (2021) 229537.
[32] S.W. Baek, M. Saber, A. Van der Ven, L. Pilon, Thermodynamic analysis and interpretative guide to entropic potential measurements of lithium-ion battery electrodes, J. Phys. Chem. C 126 (2022) 6096–6110.
[33] O. Munteshari, J. Lau, A. Krishnan, B. Dunn, L. Pilon, Isothermal calorimeter for measurements of time-dependent heat generation rate in individual supercapacitor electrodes, J. Power Sources 374 (2018) 257–268.
[34] G. Assat, S.L. Glazier, C. Delacourt, J.-M. Tarascon, Probing the thermal effects of voltage hysteresis in anionic redox-based lithium-rich cathodes using isothermal calorimetry, Nat. Energy 4 (2019) 647–656.
[35] A. Van der Ven, M.K. Aydinol, G. Ceder, G. Kresse, J. Hafner, First-principles investigation of phase stability in Li_xCoO_2, Phys. Rev. B 58 (1998) 2975–2987.
[36] S.W. Baek, K.E. Wyckoff, D.D. Robertson, M. Frajnkovič, Y. Zhou, S.H. Tolbert, R. Seshadri, L. Pilon, Operando calorimetry investigation of particle size effects on heat generation in Wadsley–Roth $(W_{0.2}V_{0.8})_3O_7$-based electrodes, ACS Appl. Energy Mater. 6 (2023) 1355–1367.
[37] Y. Zhou, E. Le Calvez, S.W. Baek, M. Frajnkovič, C. Douard, E. Gautron, O. Crosnier, T. Brousse, L. Pilon, Effect of particle size on thermodynamics and lithium ion transport in electrodes made of $TiNb_2O_9$ microparticles or nanoparticles, Energy Storage Mater. 52 (2022) 371–385.